Supplementary Information

A multifunctional quasi-solid-state polymer electrolyte with highly selective ion highways for practical zinc ion batteries

Chengwu Yang[1,2#]*, Pattaraporn Woottapanit[1#], Sining Geng[2], Rungroj Chanajaree[3], Yue Shen[4], Kittima Lolupiman[1], Wanwisa Limphirat[5], Teerachote Pakornchote[6], Thiti Bovornratanaraks[6], Xinyu Zhang[2]*, Jiaqian Qin[1]*, Yunhui Huang[4]*

[1]Center of Excellence in Responsive Wearable Materials, Department of Materials Science, Faculty of Science, Chulalongkorn University, Bangkok 10330, Thailand

[2]State Key Laboratory of Metastable Materials Science and Technology, Yanshan University, Qinhuangdao 066004, P. R. China

[3]Metallurgy and Materials Science Research Institute, Chulalongkorn University, Bangkok 10330, Thailand

[4]State Key Laboratory of Materials Processing and Die & Mould Technology, School of Materials Science and Engineering, Huazhong University of Science and Technology, Wuhan, 430074, China

[5]Synchrotron Light Research Institute (Public Organization), Nakhon Ratchasima 30000, Thailand

[6]Extreme Conditions Physics Research Laboratory, Physics of Energy Materials Research Unit, Department of Physics, Faculty of Science, Chulalongkorn University, Bangkok, 10330, Thailand

[#] These authors contributed equally to this work.

*Corresponding Author. E-mail: chengwu.y@chula.ac.th (C. Yang), jiaqian.q@chula.ac.th (J. Qin), xyzhang@ysu.edu.cn (X. Zhang),

huangyh@hust.edu.cn (Y. Huang)

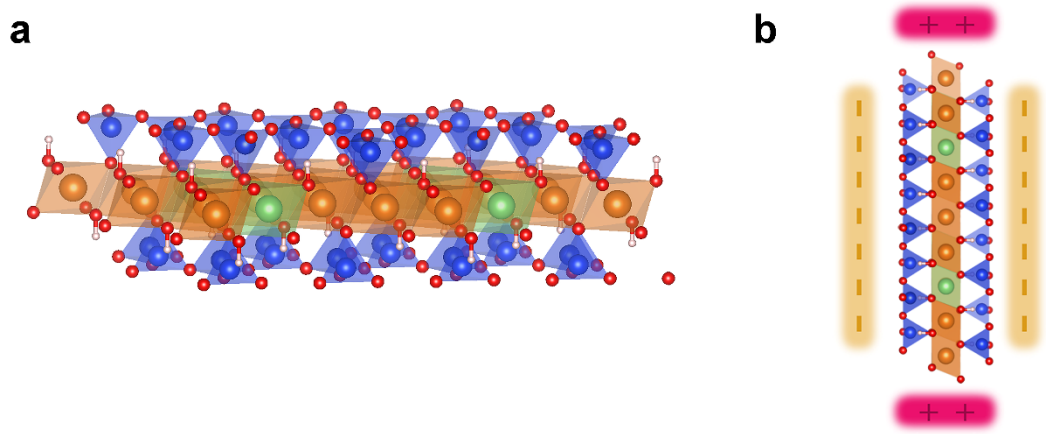

Supplementary Fig. S1 (a) The structure of LMS platelet, in which the red, blue, pink, yellow and green balls represent O, Si, H, Mg, and Li atoms. (b) The charge distribution in LMS.

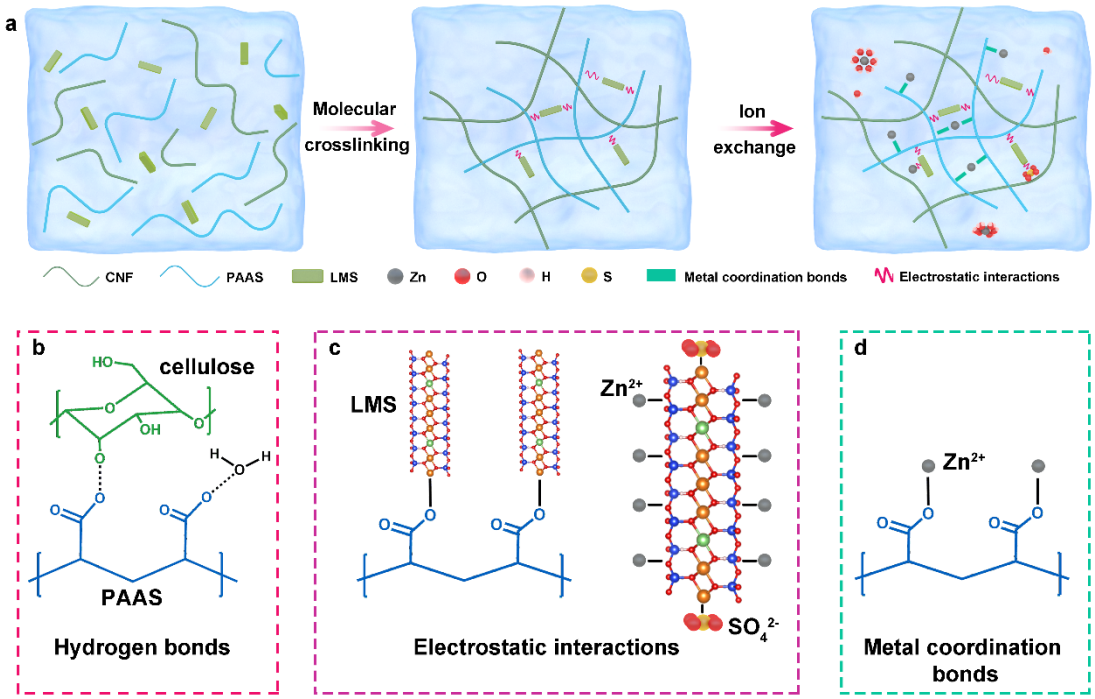

Supplementary Fig. S2 (a) Schematic illustration of the synthetic process of the PLCZ electrolyte. The interactions between molecules and between molecule and ions. (b) The formed hydrogen bonds. (c) The electrostatic interactions between PAAS and LMS and between LMS and Zn^{2+} ion and $SO4^{2-}$ ion. (d) The metal coordination bonds between PAAS and Zn^{2+} ion.

Supplementary Fig. S3 The digital photo of the polymer film after dried the PAAS-LMS-CNF solution.

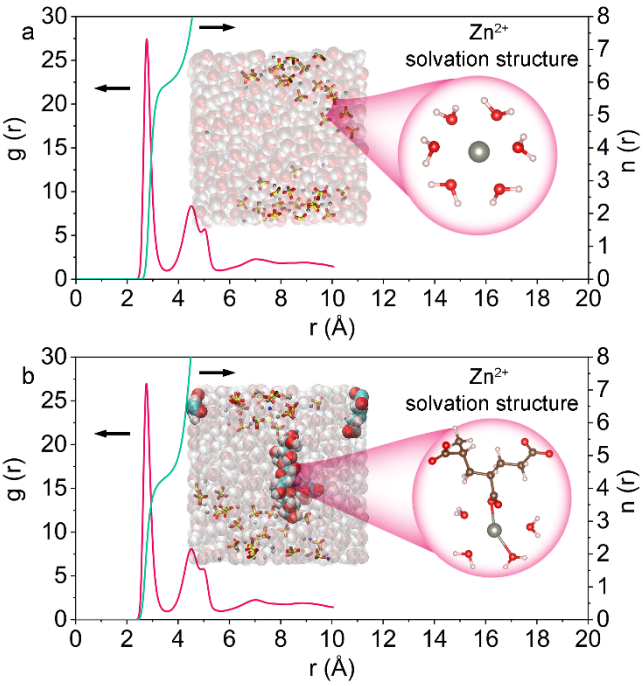

Supplementary Fig. S4 The simulated RDF of Zn^{2+}-O (H_2O) and the coordination numbers of Zn^{2+} with water molecules with the corresponding Zn^{2+} solvation structure in the (a) CZ and (b) PCZ electrolytes.

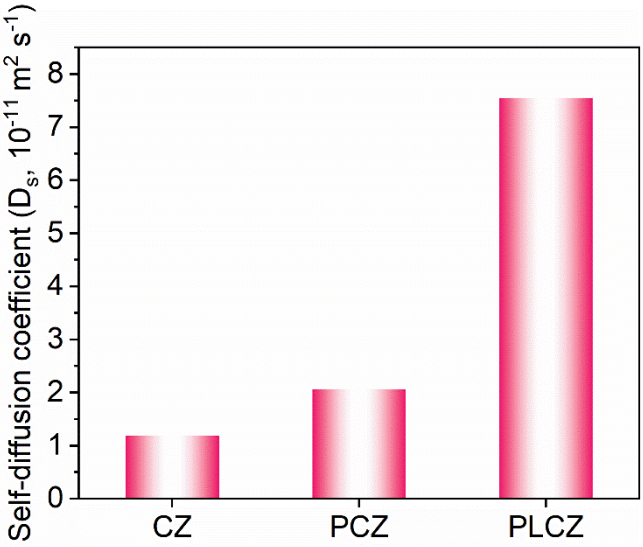

Supplementary Fig. S5 The D_s of Zn^{2+} in the CZ, PCZ and PLCZ electrolytes.

Supplementary Fig. S6 The digital photograph of PLCZ without $ZnSO_4$ immersion after strain-stress test. The weight for strain-stress test is 686 g.

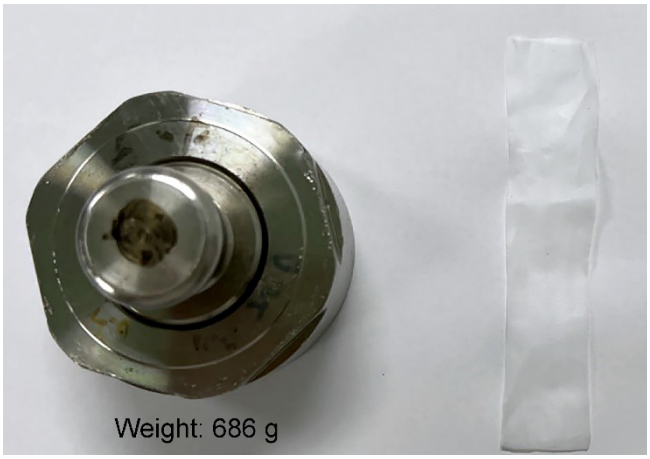

Supplementary Fig. S7 The digital photograph of PLCZ with $ZnSO_4$ immersion after strain-stress test. The weight for strain-stress test is 686 g.

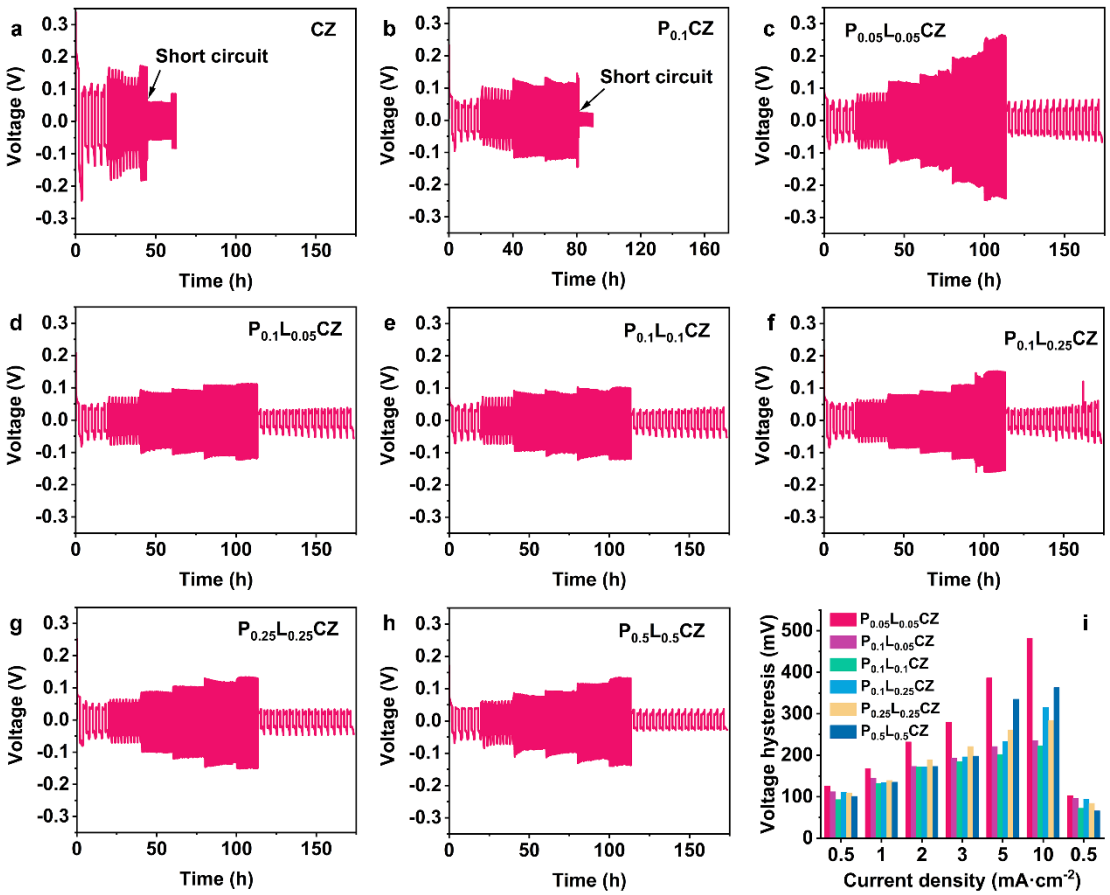

Supplementary Fig. S8 Rate performances of (a) CZ, (b) PCZ, (c) $P_{0.05}L_{0.05}CZ$, (d) $P_{0.1}L_{0.05}CZ$, (e) $P_{0.1}L_{0.1}CZ$, (f) $P_{0.1}L_{0.25}CZ$, (g) $P_{0.25}L_{0.25}CZ$ and (h) $P_{0.5}L_{0.5}CZ$ at the current densities of 0.5, 1, 2, 3, 5, 10 and 0.5 mA cm^{-2}. (i) The voltage hysteresis of each electrolyte at various current density.

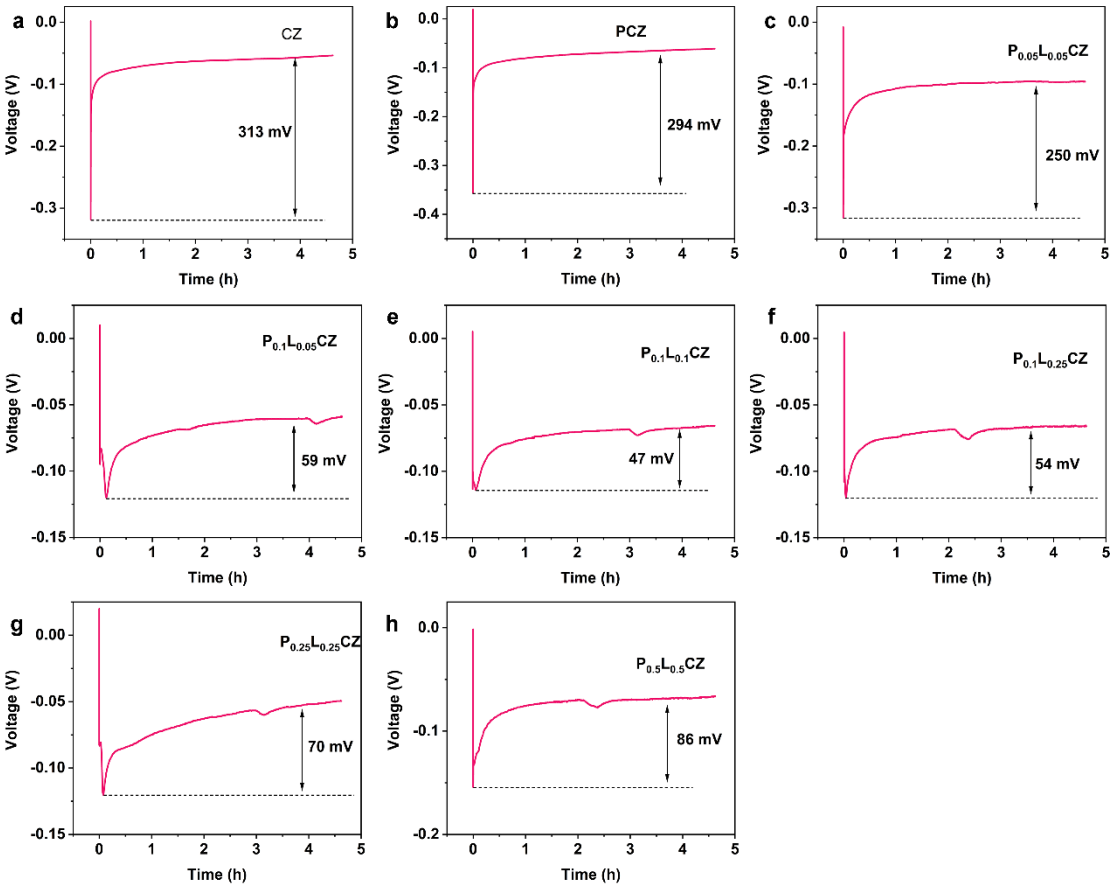

Supplementary Fig. S9 The Zn nucleation overpotential of Zn^{2+} on Zn anodes with (a) CZ, (b) PCZ, (c) $P_{0.05}L_{0.05}CZ$, (d) $P_{0.1}L_{0.05}CZ$, (e) $P_{0.1}L_{0.1}CZ$, (f) $P_{0.1}L_{0.25}CZ$, (g) $P_{0.25}L_{0.25}CZ$ and (h) $P_{0.5}L_{0.5}CZ$.

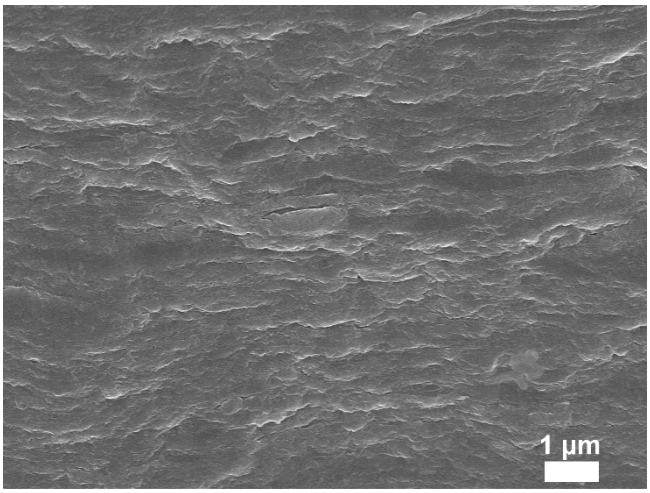

Supplementary Fig. S10 SEM image of PLCZ at cross-sectional view with the enlarged photo. The $P_{0.1}L_{0.1}CZ$ shows firm and compact texture structure.

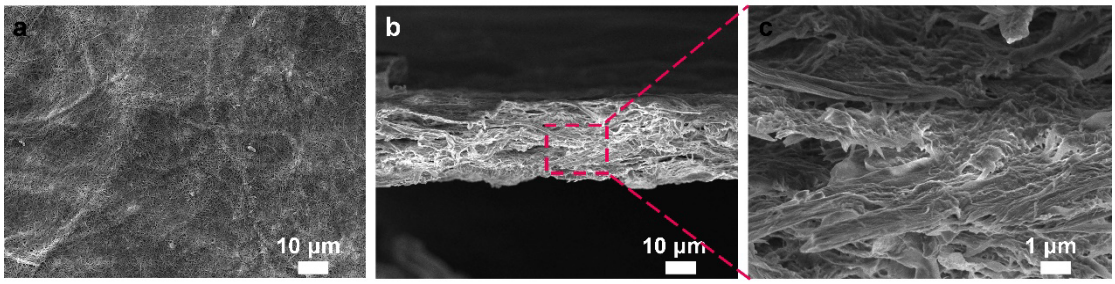

Supplementary Fig. S11 SEM image of CNF separator after soaking $ZnSO_4$ electrolyte at (a) top view and (b, c) cross-sectional view.

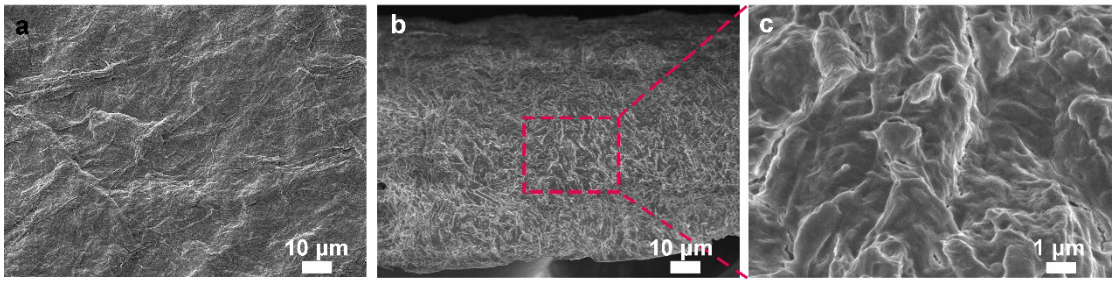

Supplementary Fig. S12 SEM image of PCZ at (a) top view and (b, c) cross-sectional view.

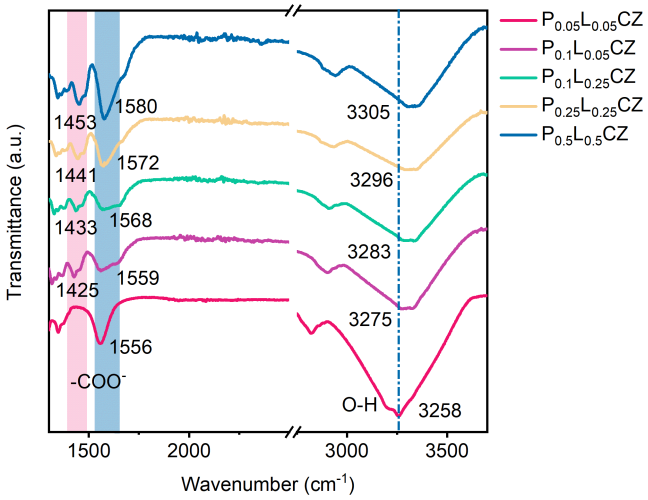

Supplementary Fig. S13 FTIR spectra of $P_{0.05}L_{0.05}CZ$, $P_{0.1}L_{0.05}CZ$, $P_{0.1}L_{0.5}CZ$, $P_{0.25}L_{0.25}CZ$ and $P_{0.5}L_{0.5}CZ$.

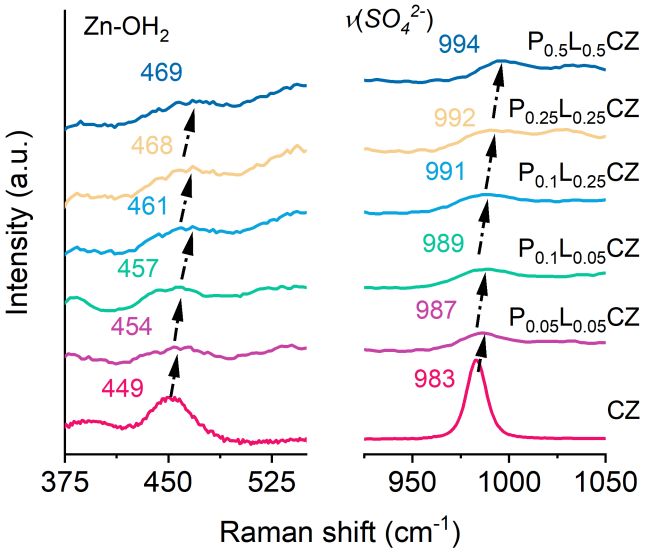

Supplementary Fig. S14 Raman spectra of $P_{0.05}L_{0.05}CZ$, $P_{0.1}L_{0.05}CZ$, $P_{0.1}L_{0.25}CZ$, $P_{0.25}L_{0.25}CZ$ and $P_{0.5}L_{0.5}CZ$.

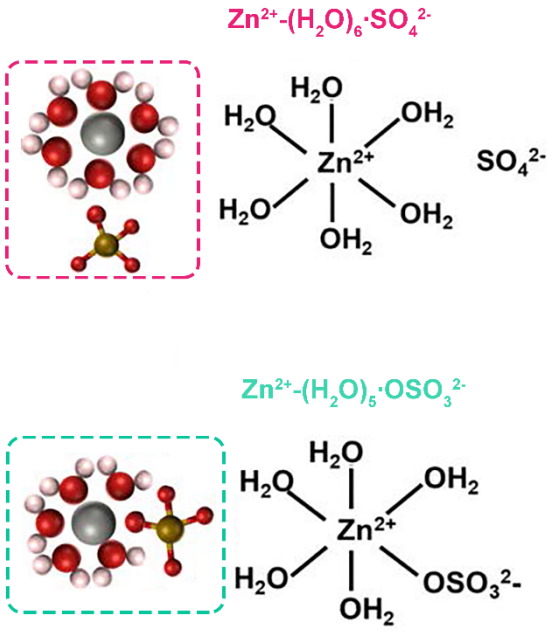

Supplementary Fig. S15 The solvation structures in electrolytes.

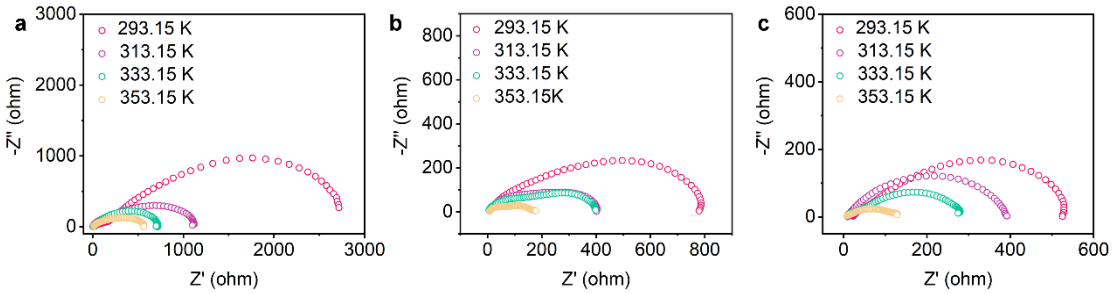

Supplementary Fig. S16 EIS plots of Zn||Zn symmetric cells with (a) CZ, (b) PCZ and (c) PLCZ at different temperatures.

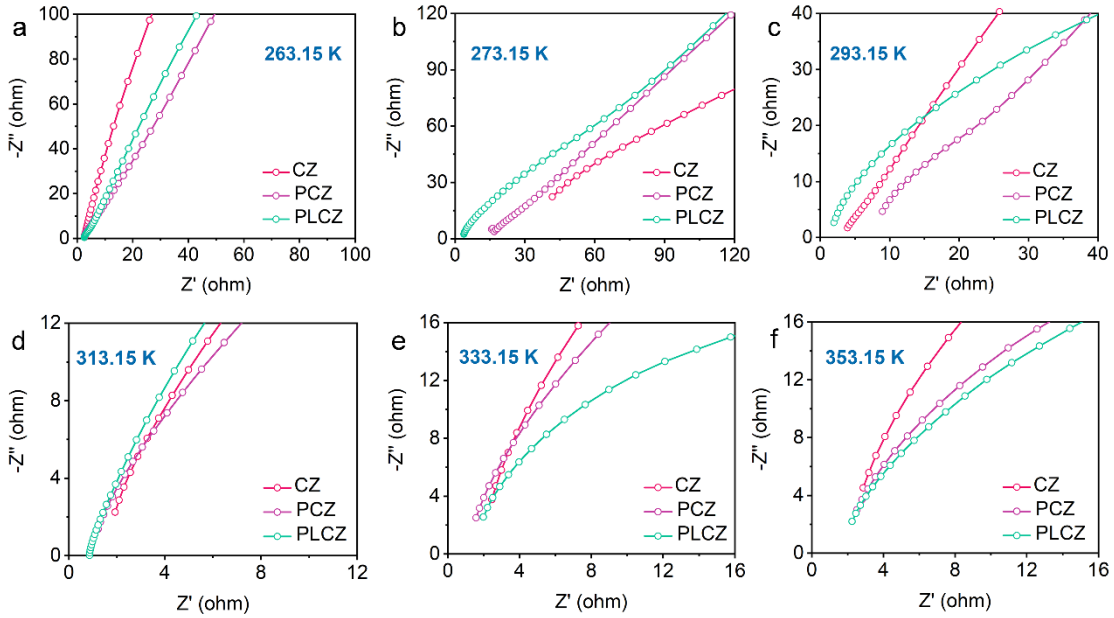

Supplementary Fig. S17 EIS plots of CZ, PCZ and PLCZ at (a) 263.15 K, (b) 273.15 K, (c) 293.15 K, (d) 313.15 K, (e) 333.15 K, and (f) 353.15 K.

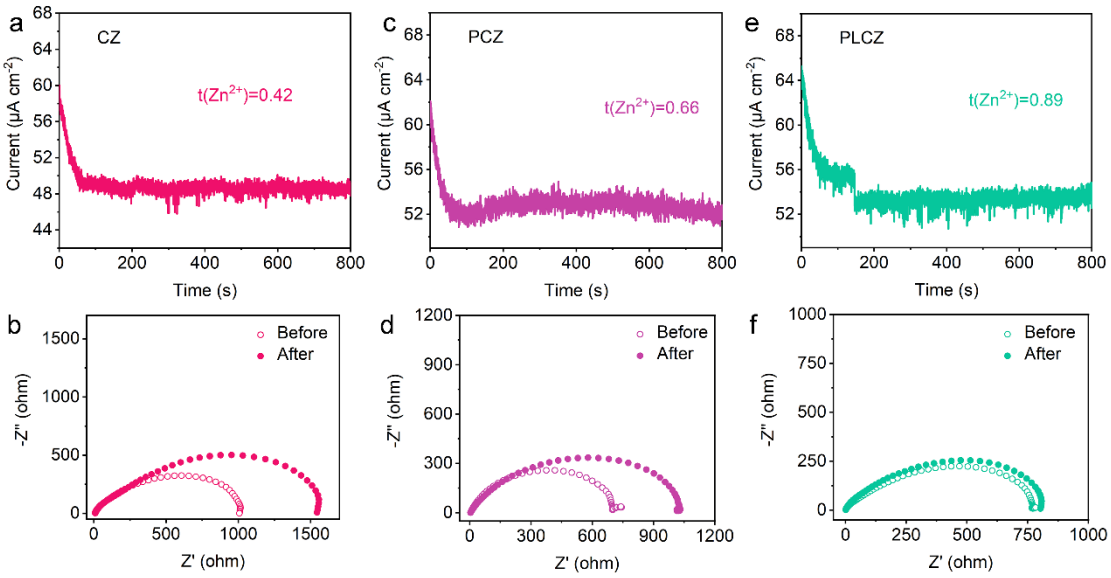

Supplementary Fig. S18 CA curves and the corresponding EIS plots before and after CA of Zn||Zn symmetric cells. (a, b) CZ, (c, d) PCZ and (e, f) PLCZ.

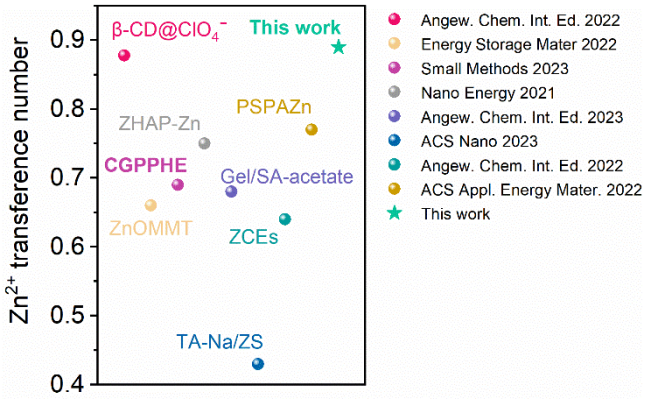

Supplementary Fig. S19 The comparison of Zn^{2+} transference number with the reported liquid and solid-state electrolytes.

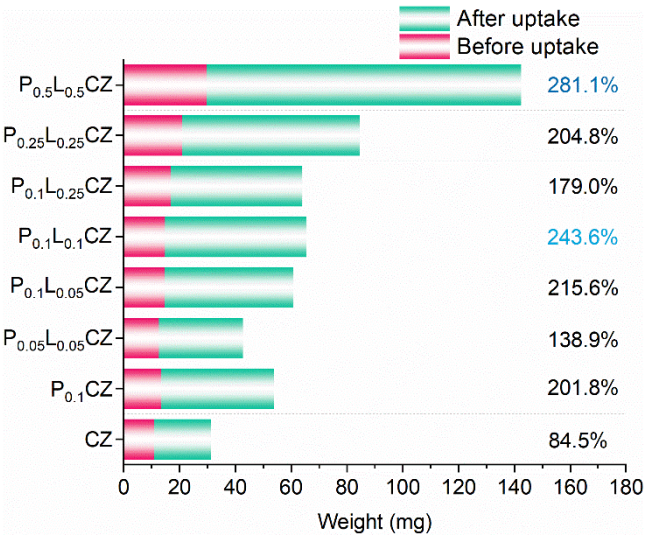

Supplementary Fig. S20 Electrolyte uptake of CNF separator and all polymer films. After immersed, the CZ sample shows low electrolyte uptake of 84.5 %, while the $P_{0.1}L_{0.1}CZ$ has higher electrolyte uptake of 243.6 %.

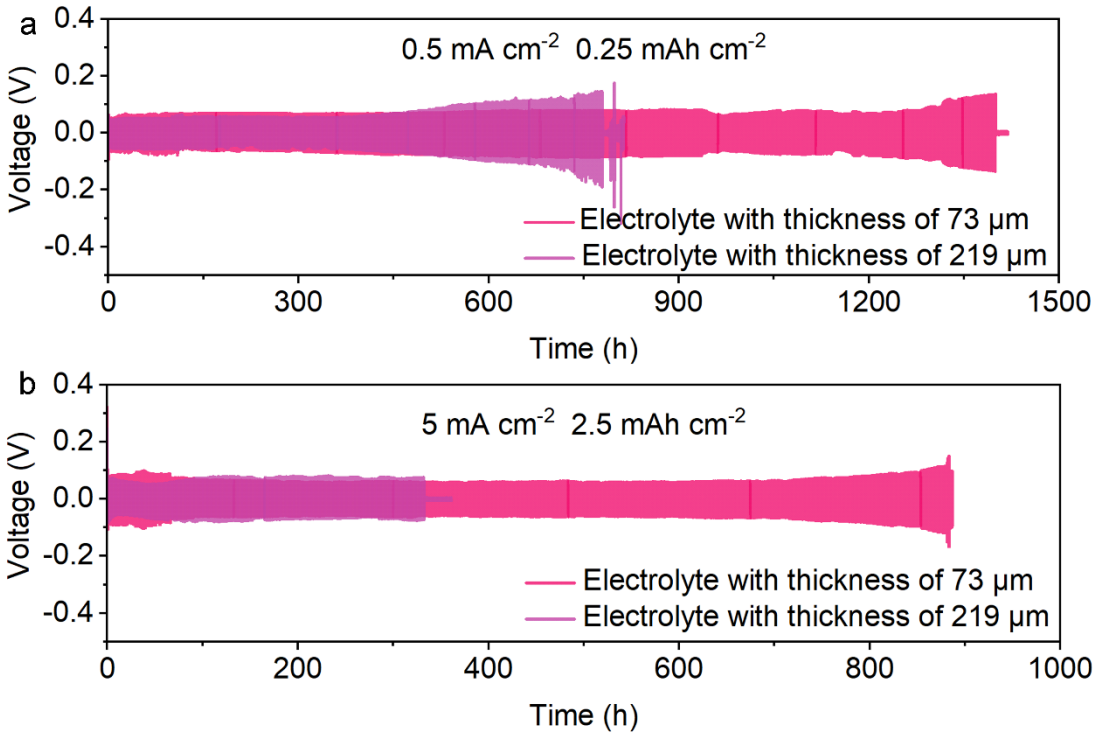

Supplementary Fig. S21 Galvanostatic cycling of the PLCZ cells with the electrolyte thicknesses of 73 and 219 μm at (a) 0.5 mA cm^{-2}, 0.25 mAh cm^{-2} and (b) 5 mA cm^{-2}, 2.5 mAh cm^{-2}. The electrolyte thickness is regulated by controlling the used volume of the PAAS-LMS-CNF solution in which the mass ratio between PAAS, LMS and CNF is 0.1:0.1:30. When the volume of the PAAS-LMS-CNF solution is 70, 140, 280 ml, the electrolyte thickness is 73, 128 and 219 μm, respectively.

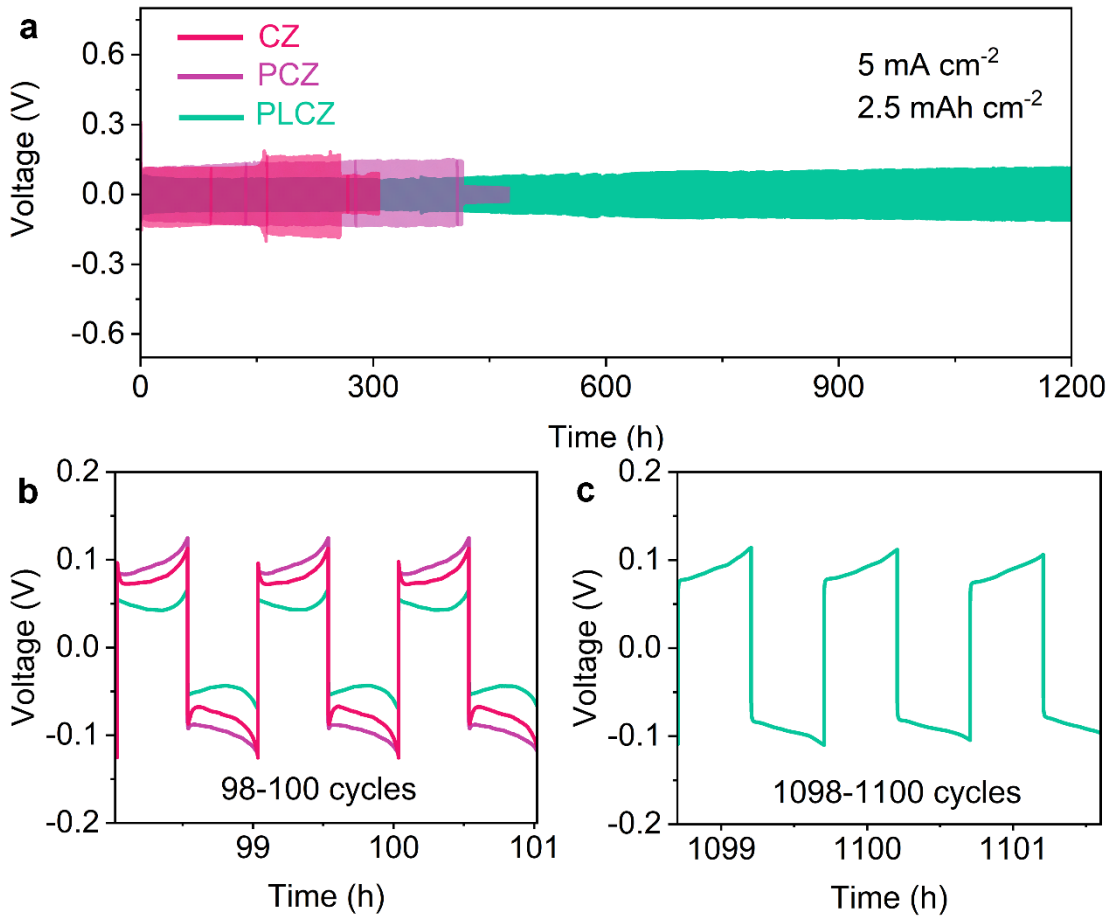

Supplementary Fig. S22 (a) Galvanostatic cycling of Zn||Zn cells with CZ, PCZ and PLCZ at 5 mA cm^{-2}/2.5 mAh cm^{-2}. The voltage-time profile of Zn||Zn cells at (b) 98-100 cycles and (c) 1098-1100 cycles.

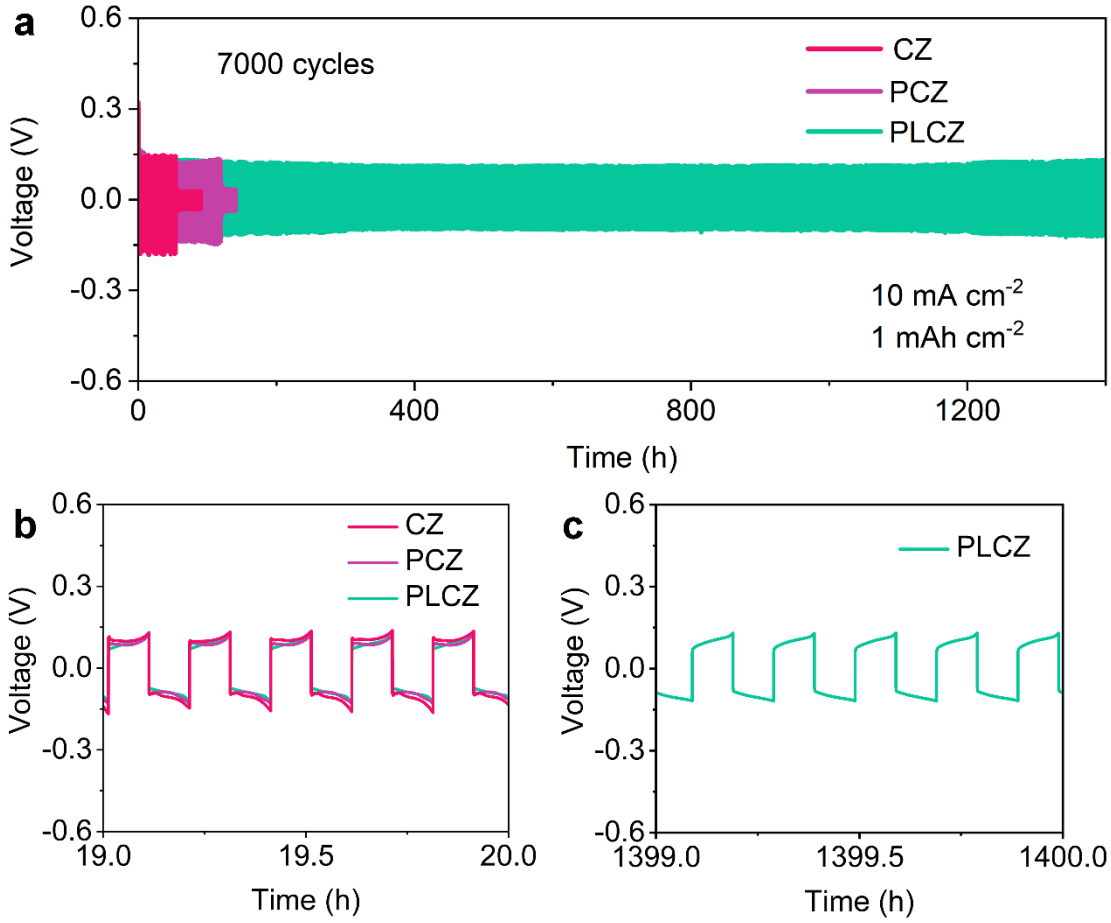

Supplementary Fig. S23 (a) Galvanostatic cycling of Zn||Zn cells with CZ, PCZ and PLCZ at 10 mA cm^{-2}/1 mAh cm^{-2}. The voltage-time profile of Zn||Zn cells at (b) 91-95 cycles and (c) 6996-7000 cycles.

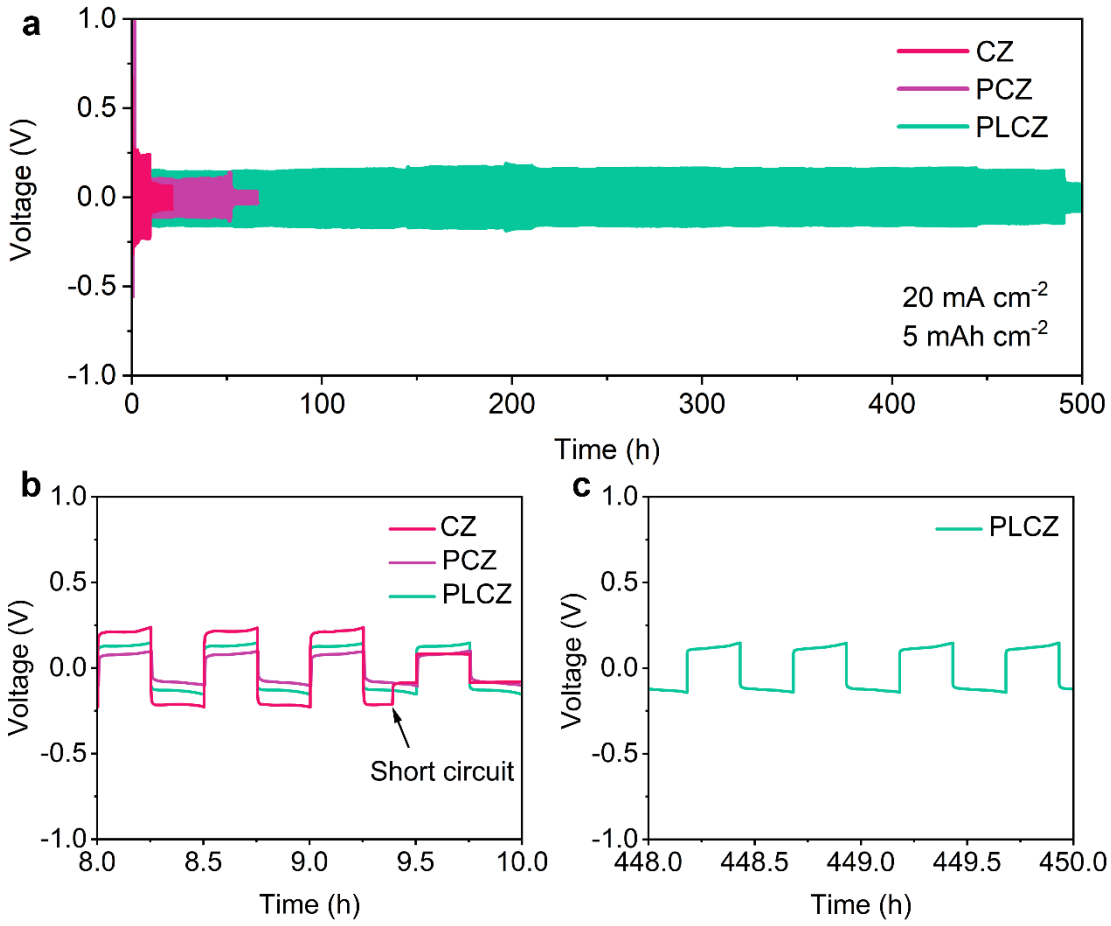

Supplementary Fig. S24 (a) Galvanostatic cycling of Zn||Zn cells with CZ, PCZ and PLCZ at 20 mA cm^{-2}/5 mAh cm^{-2}. The voltage-time profile of Zn||Zn cells at (b) 17-20 cycles and (c) 897-900 cycles.

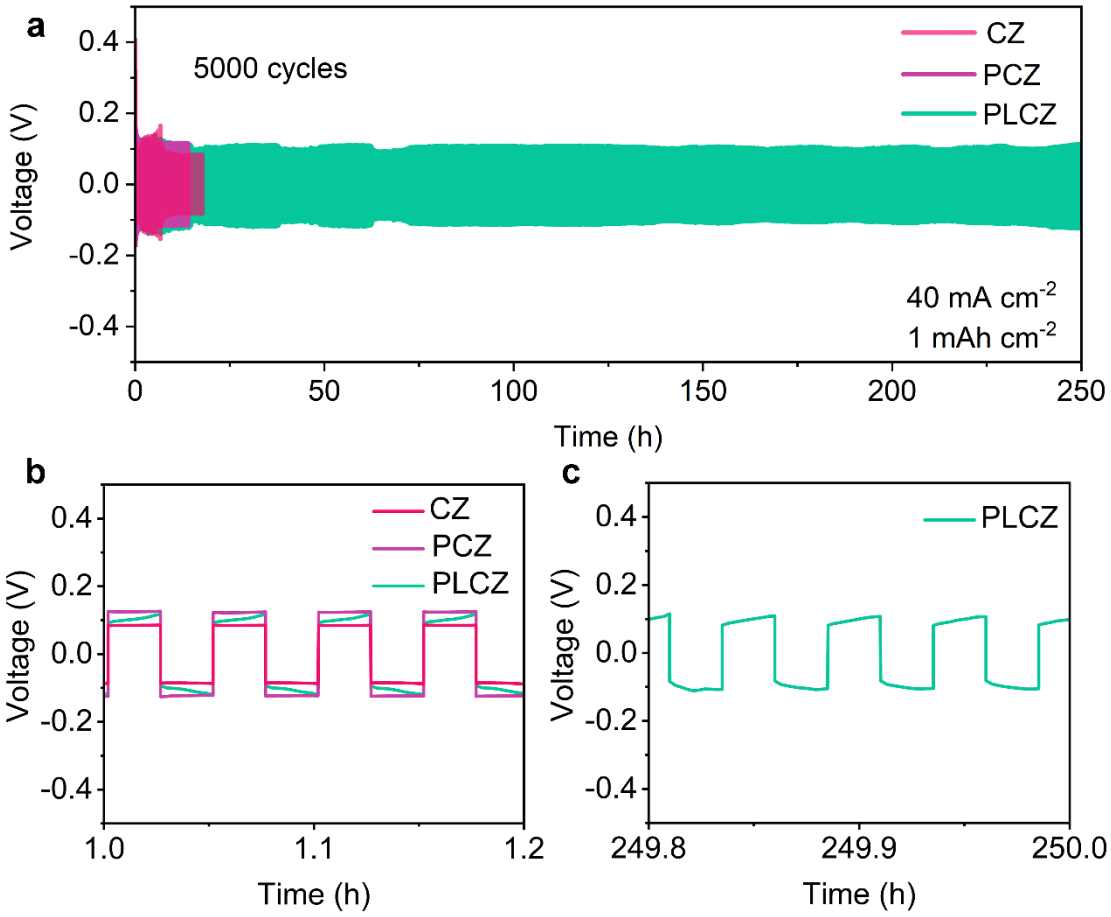

Supplementary Fig. S25 (a) Galvanostatic cycling of Zn||Zn cells with CZ, PCZ and PLCZ at 40 mA cm^{-2}/1 mAh cm^{-2}. The voltage-time profile of Zn||Zn cells at (b) 21-24 cycles and (c) 4997-5000 cycles.

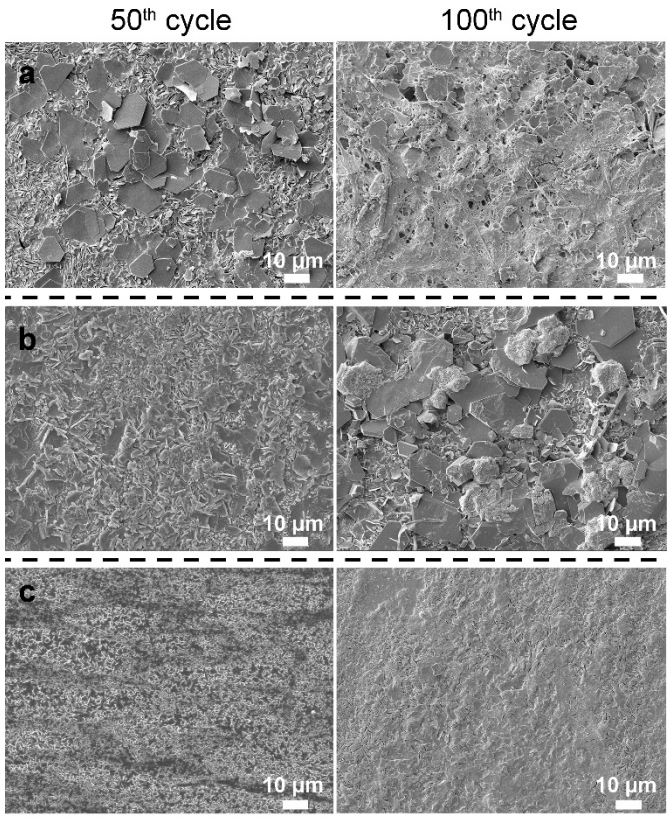

Supplementary Fig. S26 SEM images of Zn anode with (a) CZ, (b) PCZ and (c) PLCZ after 50 and 100 cycles.

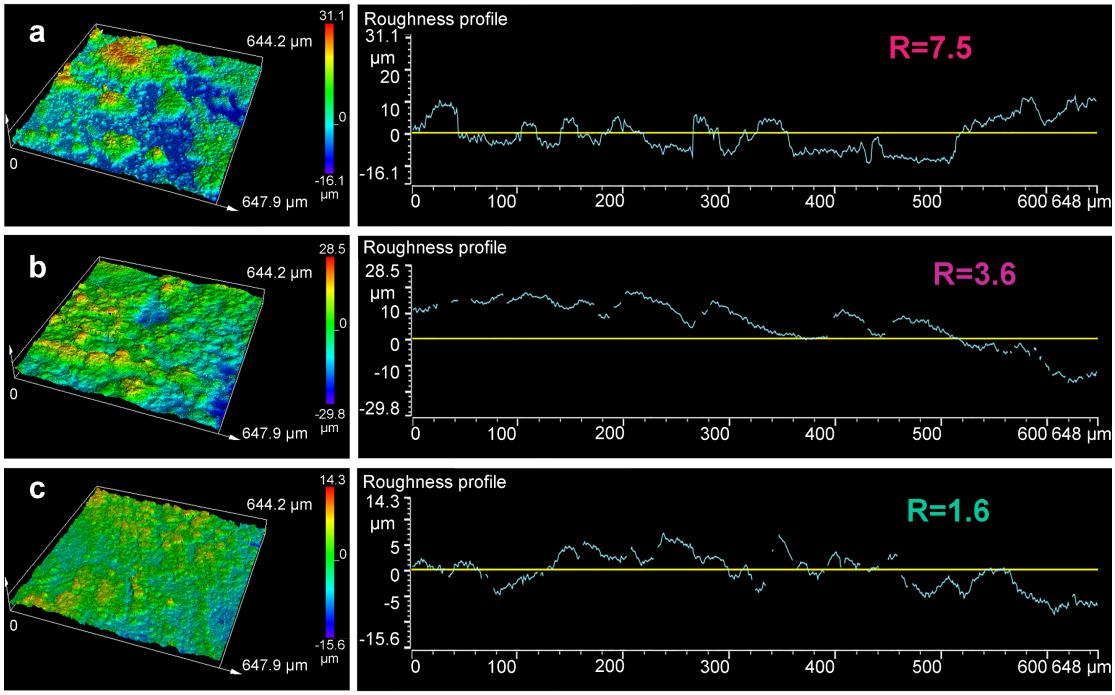

Supplementary Fig. S27 Confocal images of Zn anodes with the surface roughness (R) after 200 cycles. (a) CZ, (b) PCZ and (c) PLCZ.

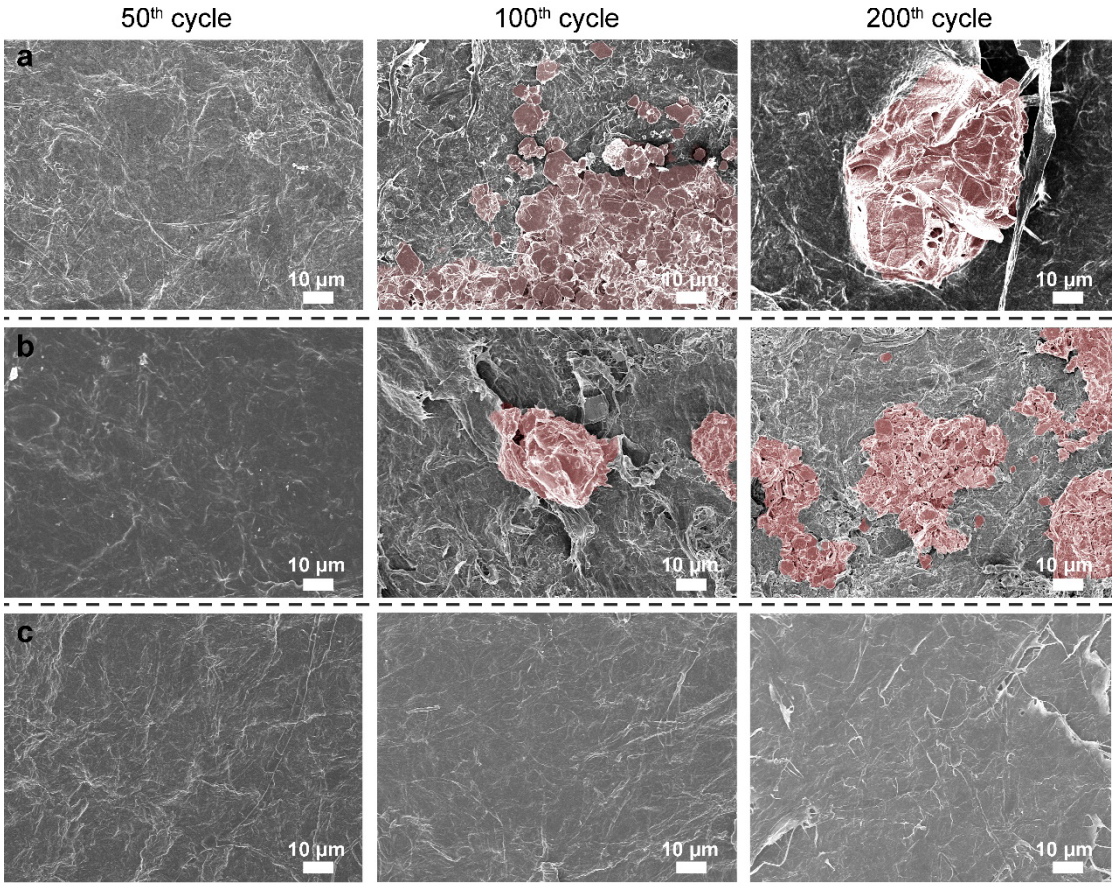

Supplementary Fig. S28 SEM images of (a) CZ, (b) PCZ and (c) PLCZ after cycling different cycles. The colored regions represent the formed Zn dendrites.

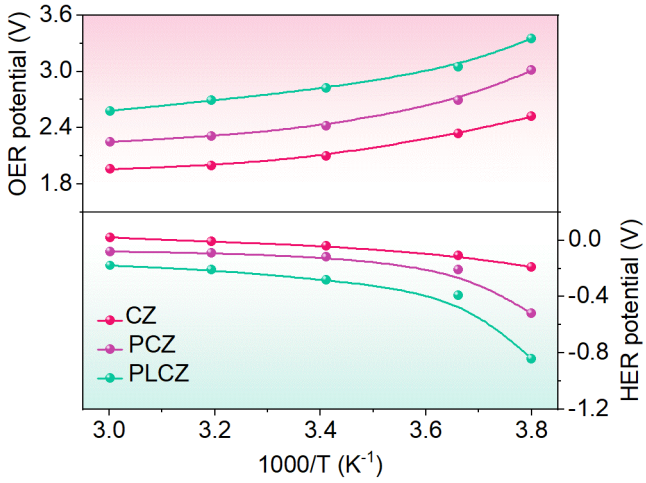

Supplementary Fig. S29 OER and HER onset potentials at different temperatures of CZ, PCZ and PLCZ.

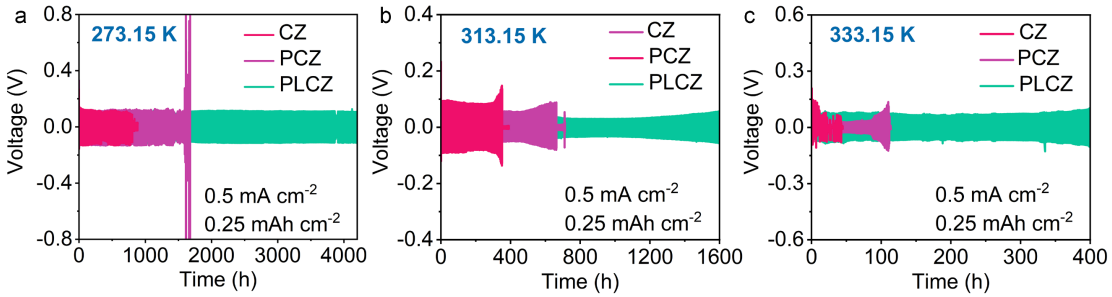

Supplementary Fig. S30 Cycling stability of Zn||Zn cells with the electrolytes at (a) 273.15, (b) 313.15 and (c) 333.15 K.

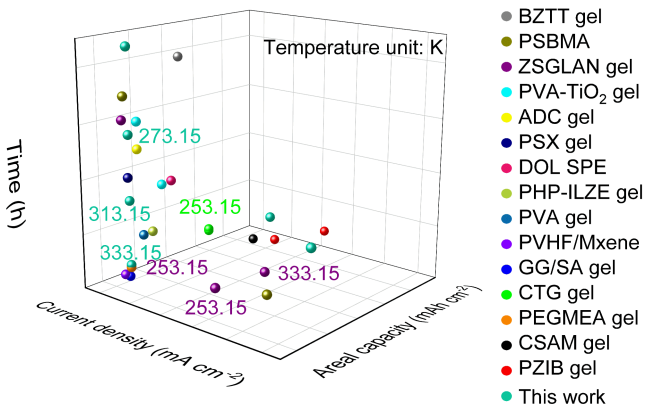

Supplementary Fig. S31 The comparison of the cycling lifespan of the electrolytes.

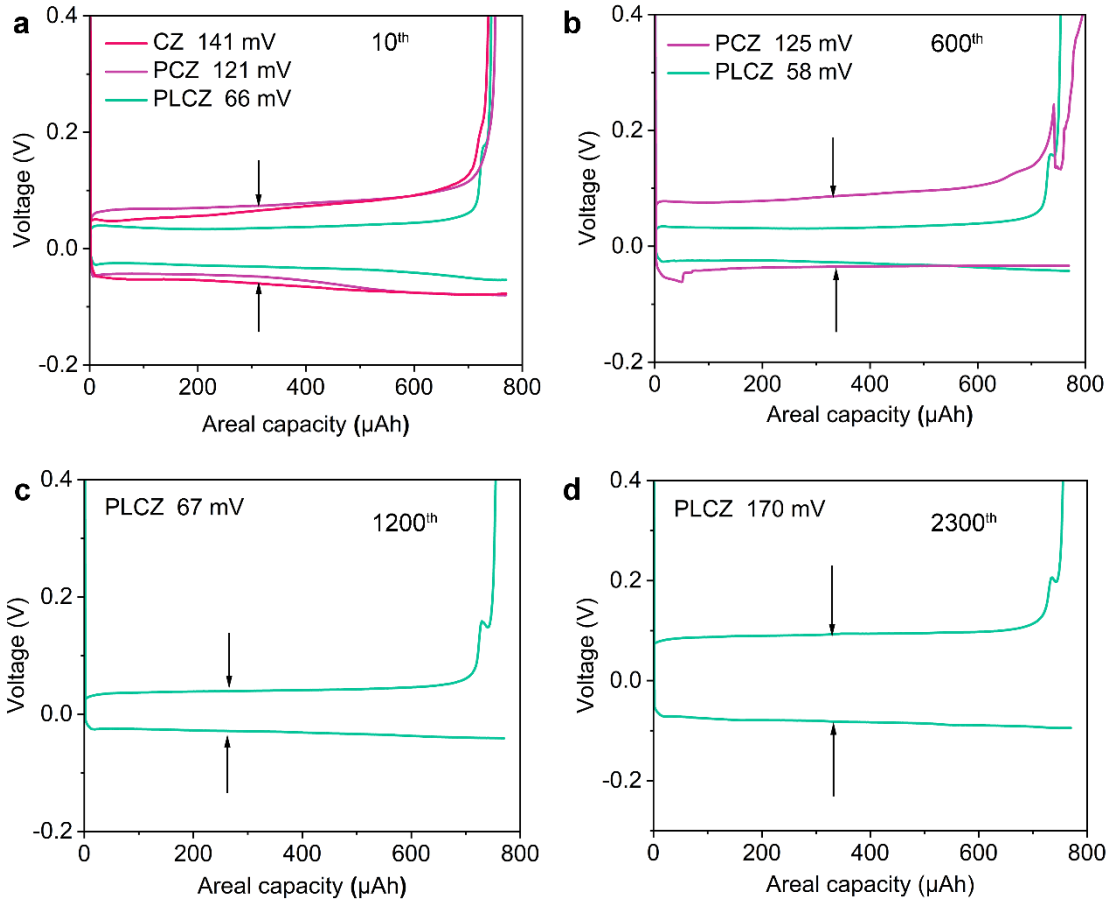

Supplementary Fig. S32 Voltage profiles of Zn||Cu asymmetric cells with CZ, PCZ and PLCZ at 1 mA·cm^{-2}/0.5 mA·cm^{-2} at different cycles. (a) 10th cycle, (b) 600th cycle, (c) 1200th cycle and (d) 2300th cycle.

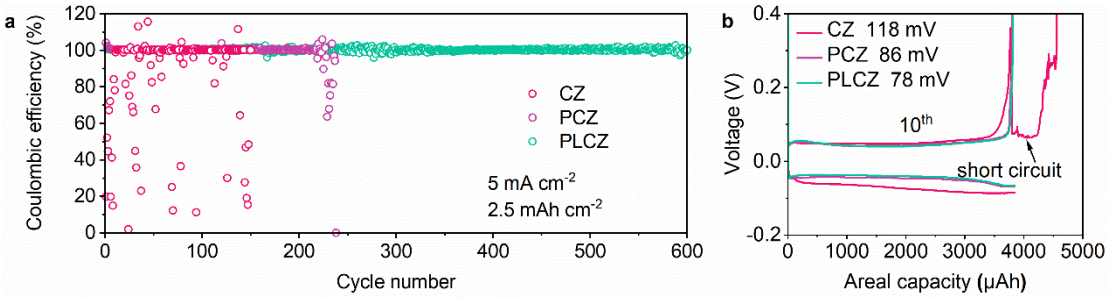

Supplementary Fig. S33 (a) Coulombic efficiency of Zn||Cu asymmetric cells with CZ, PCZ and PLCZ at 5 mA cm^{-2}/2.5 mA cm^{-2} with (b) the corresponding voltage profiles at the 10^{th} cycle.

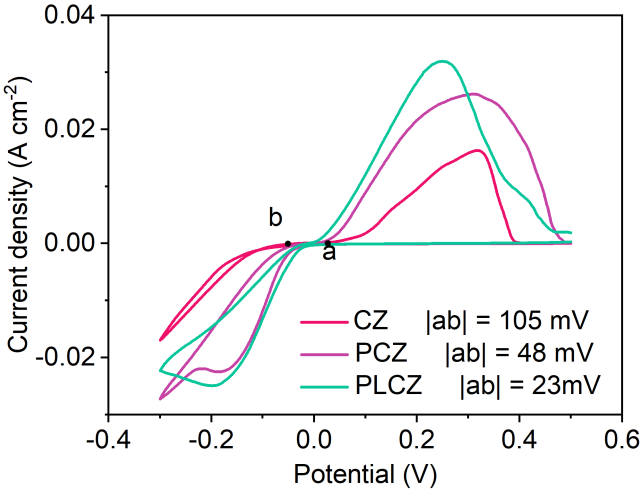

Supplementary Fig. S34 CV curves of Zn||Cu asymmetric cells with CZ, PCZ and PLCZ. The nucleation overpotential in CV curves is defined as the difference between the crossover point (point a, where the current density begins to increase from zero) and the onset point (point b) of Zn^{2+} ion reduction.

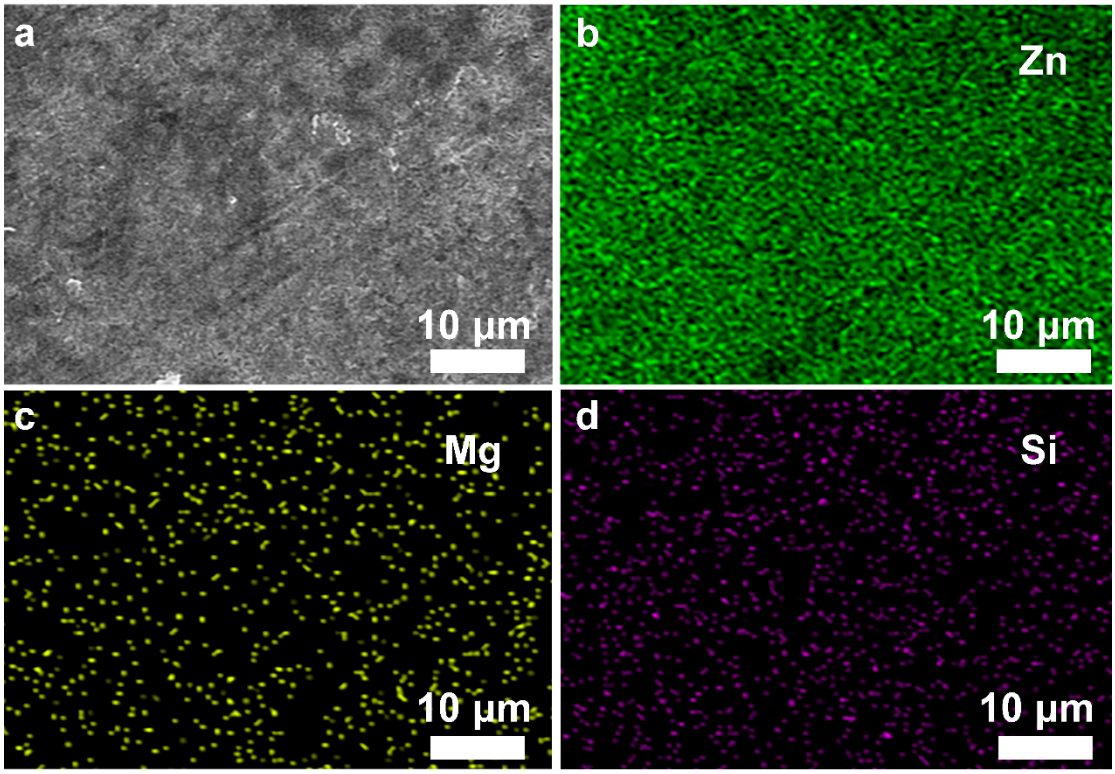

Supplementary Fig. S35 (a) SEM image of the cycled Zn anode with EDS mapping of (b) Zn, (c) Mg and (d) Si.

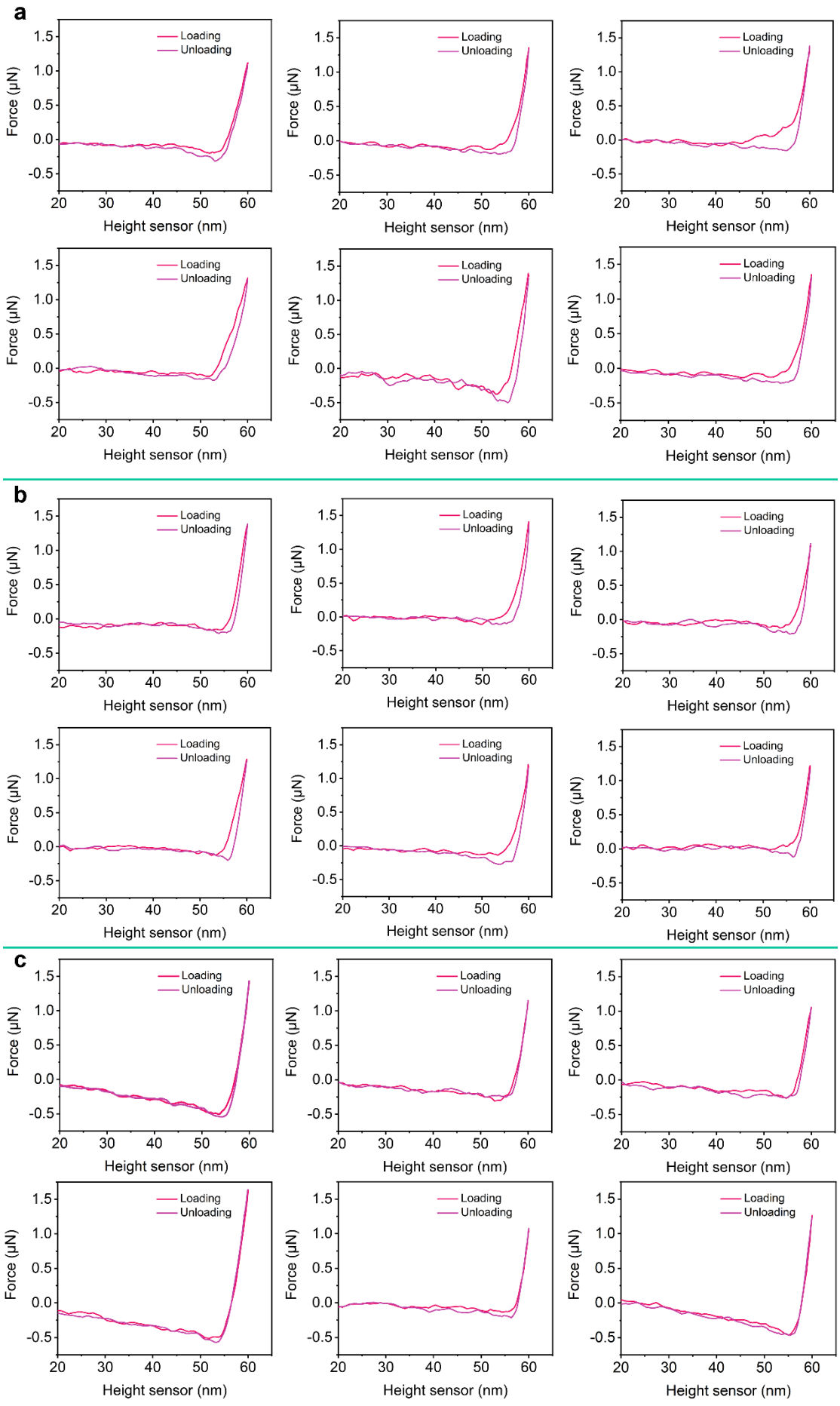
a
b
c
Loading
Unloading
Force (μN)
Height sensor (nm)
1.5
1.0
0.5
0.0
-0.5
20
30
40
50
60

Supplementary Fig. S36 The force-displacement curves for nanoindentation experiments on the Zn anodes with (a) CZ, (b) PCZ and (c) PLCZ electrolytes. Each Zn anode sample was tested 6 times for nanoindentation measurements.

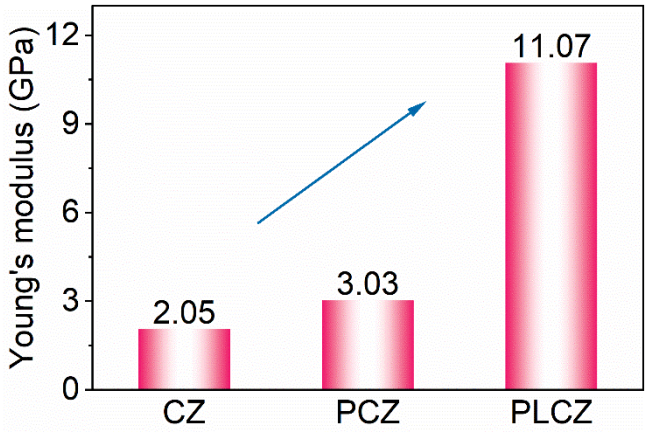

Supplementary Fig. S37 The average Young's modulus on the Zn anodes.

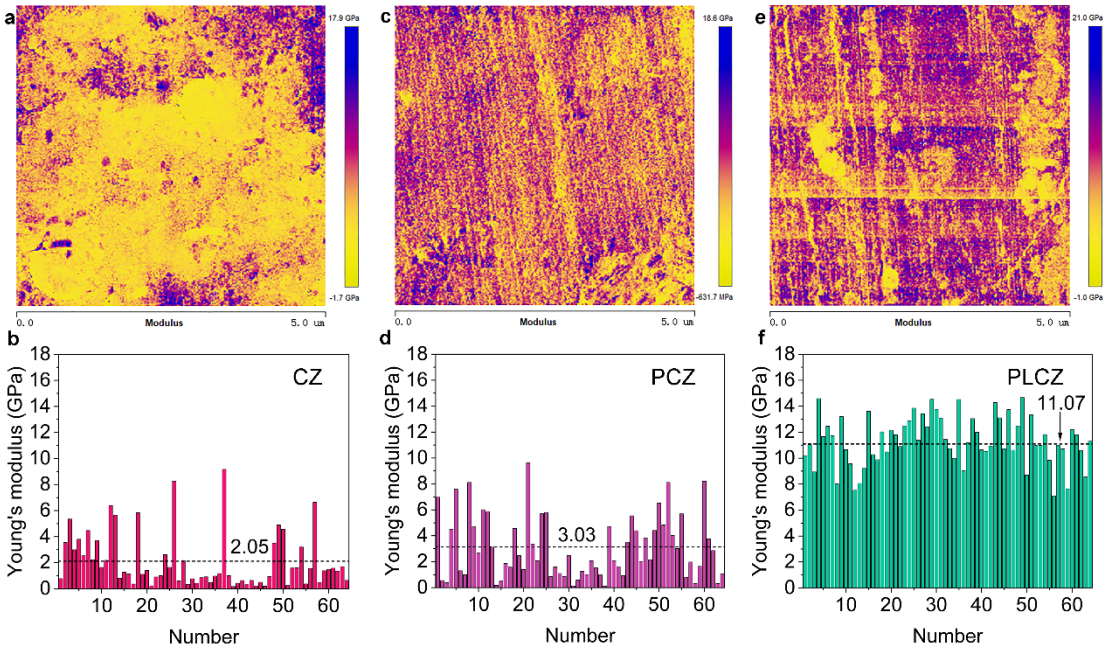

Supplementary Fig. S38 The distributions of Young' modulus with the measured values on the Zn electrodes with (a, b) CZ, (c, d) PCZ and (e, f) PLCZ. The standard error is calculated by the equation:

$$S=\sqrt{\frac{(x_1-x)^2+(x_2-x)^2+\cdots+(x_n-x)^2}{n-1}}$$

Where x_n is the value of Young's modulus; x is the average value of Young's modulus; n is the total number of Young's modulus (n=64 in this work); S is the standard error.

The calculated standard errors of the CZ, PCZ and PLCZ electrolytes are 2.07, 2.28 and 1.90 GPa, respectively. The PLCZ obtains a lower standard error, indicating a more uniform distribution of Young's modulus.

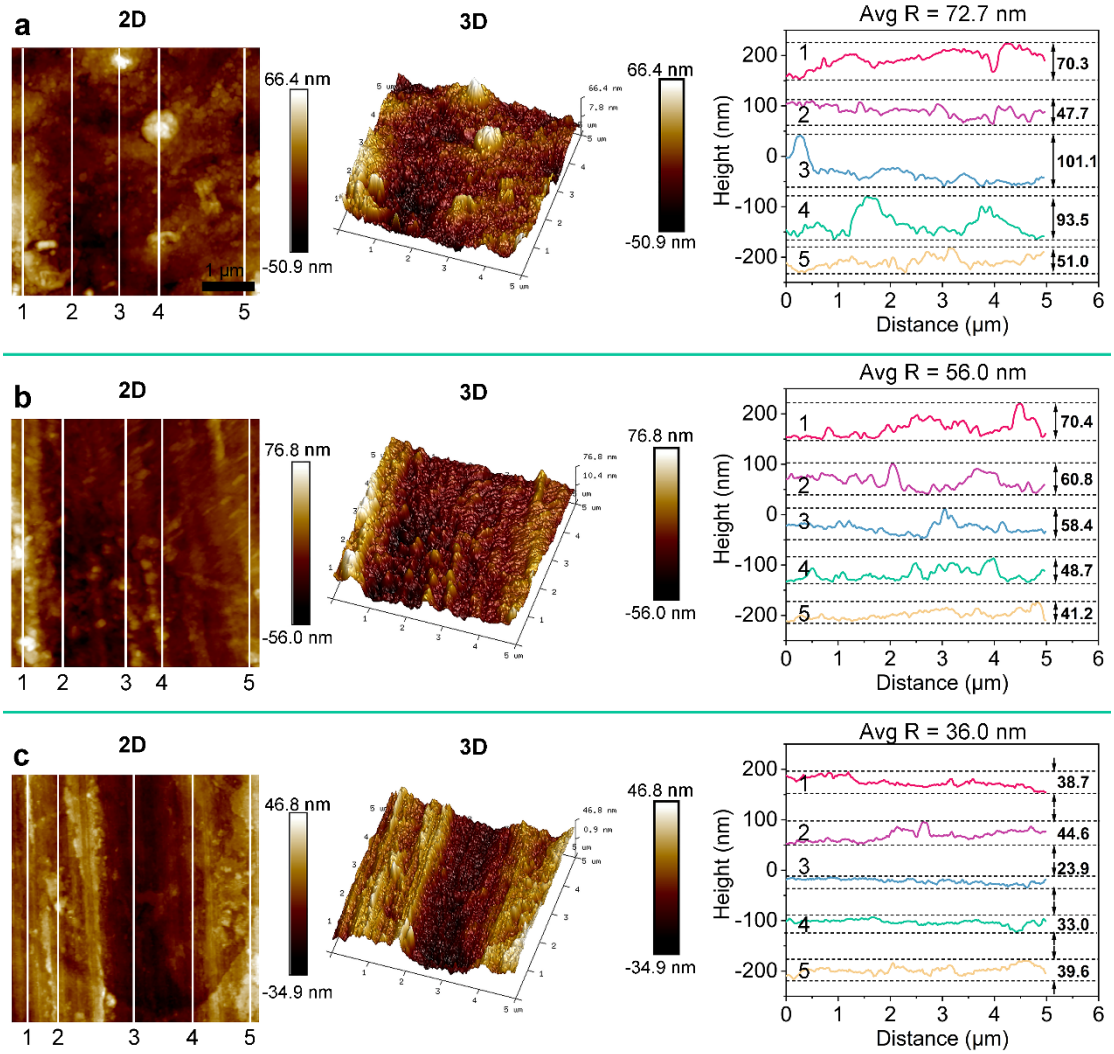

Supplementary Fig. S39 2D and 3D AFM images of Zn anodes of (a) CZ, (b) PCZ and (c) PLCZ with the corresponding roughness lines. The average roughness of the CZ, PCZ and PLCZ are 72.7, 56.0 and 36.0 nm, respectively. From AFM images and average roughness, the MEA SEI layer surface shows a better uniformity and smoothness than $Zn(OH)_2$-based SEIs.

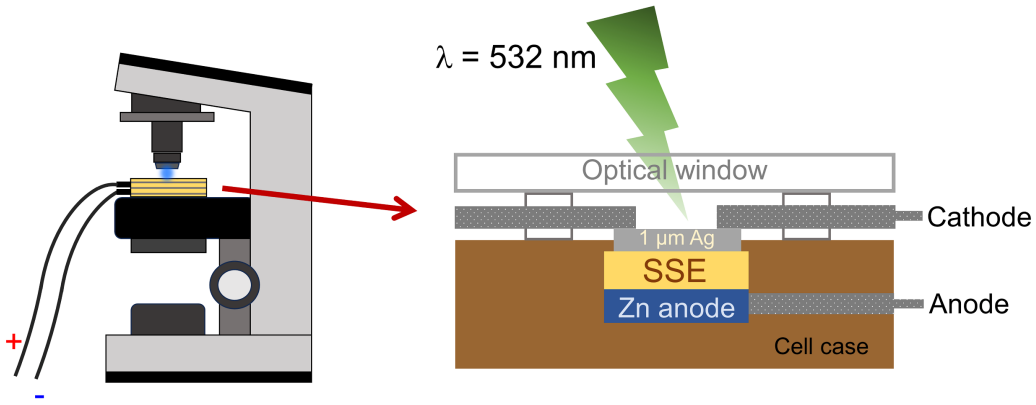

Supplementary Fig. S40 The photoelectrochemical cell for in-situ Raman spectroscopic measurements.

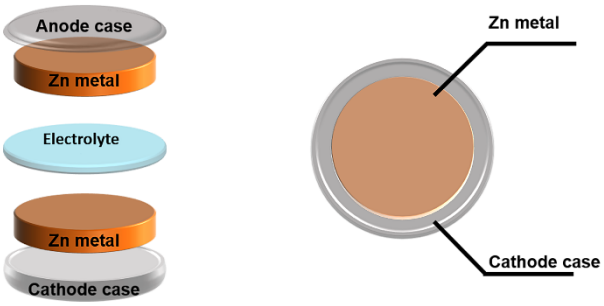

Supplementary Fig. S41 The Zn||Zn symmetric cell configuration for in-situ micro-CT test.

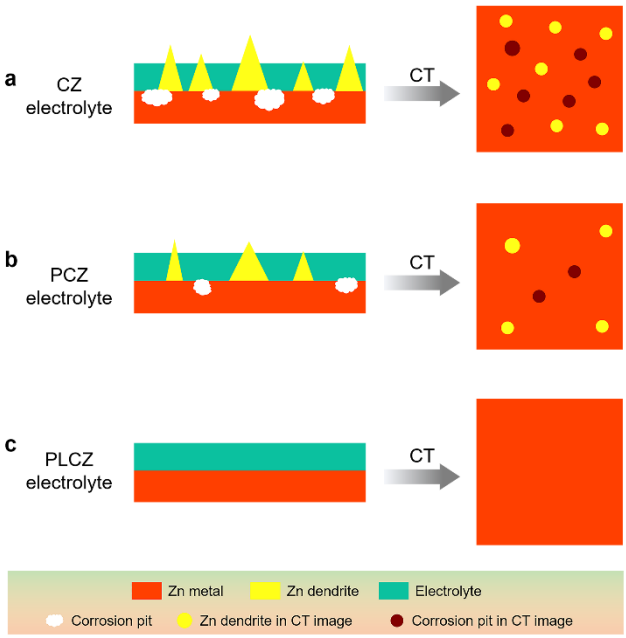

Supplementary Fig. S42 The schematic illustration of Zn dendrite growth and surface corrosion on the Zn surface (cross-sectional view) of (a) CZ, (b) PCZ and (c) PLCZ electrolytes and their corresponding micro-CT image (top view). CZ and PCZ electrolytes easily produce Zn dendrite and surface corrosion, thus the areas with Zn dendrite and surface corrosion exhibit chaotic and discontinuous color distribution. In contrast, PLCZ electrolyte effectively promotes homogeneous Zn deposition and suppresses surface corrosion, resulting in a uniform color for Zn metal electrode.

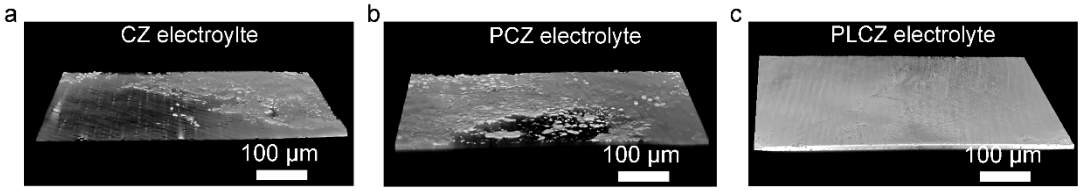

Supplementary Fig. S43 The micro-CT images of the cycled Zn anode with (a) CZ, (b) PCZ and (c) PLCZ electrolytes.

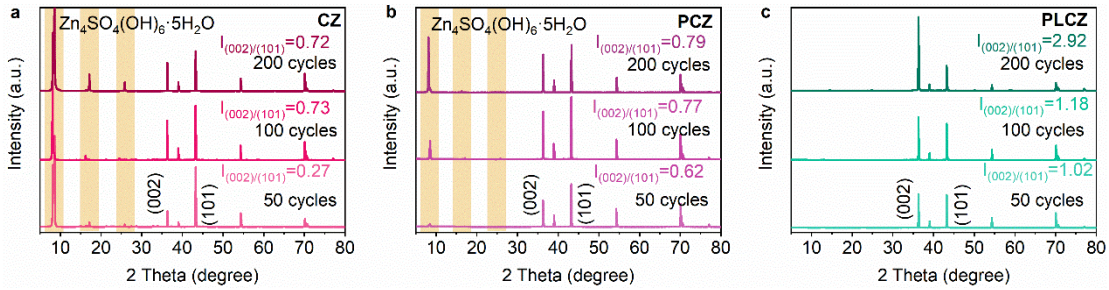

Supplementary Fig. S44 XRD patterns of Zn anodes in symmetric cells with (a) CZ, (b) PCZ and (c) PLCZ after cycling at 5 mA cm^{-2}/2.5 mAh cm^{-2}.

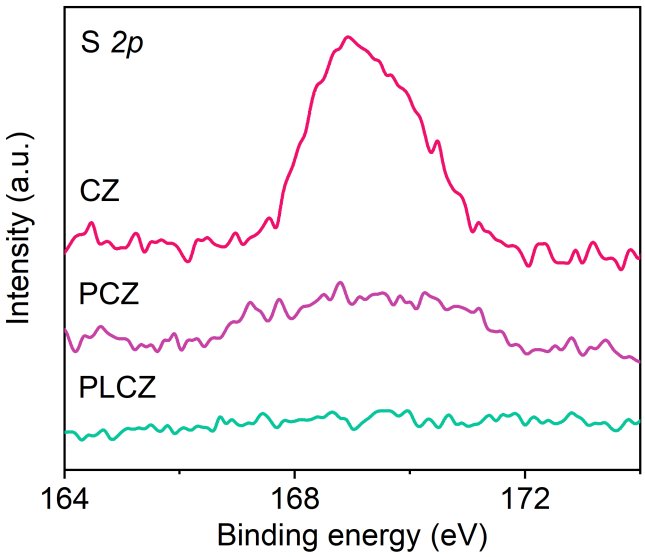

Supplementary Fig. S45 S *2p* XPS spectra of the cycled Zn anodes.

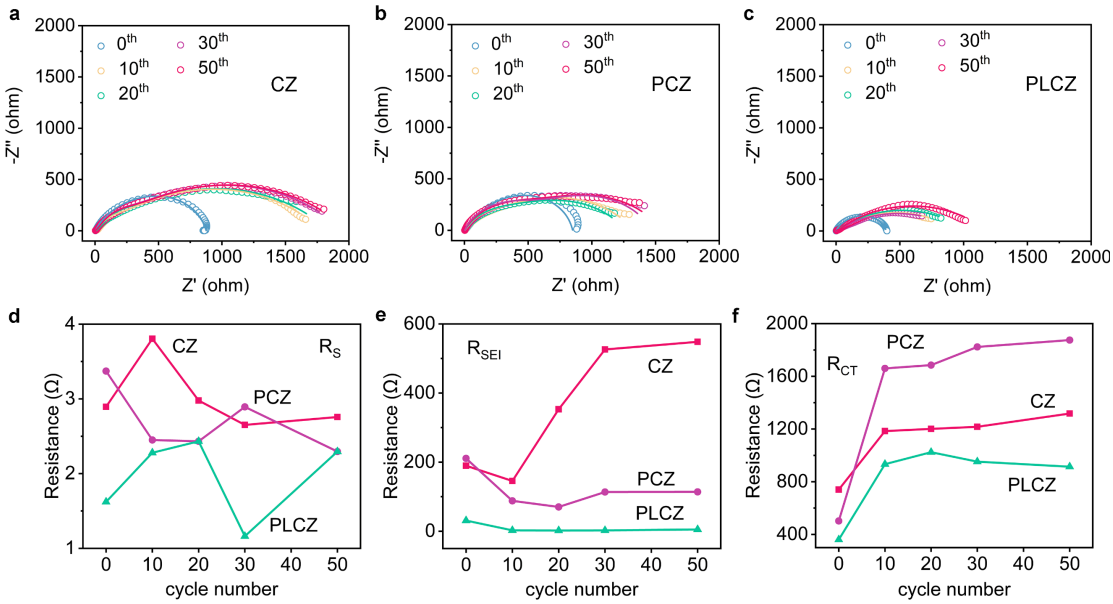

Supplementary Fig. S46 EIS plots of Zn||Zn symmetric cells with (a) CZ, (b) PCZ and (c) PLCZ after cycling different times. The solid line represents the corresponding fitted EIS plots. The calculated resistances of (d) R_s, (e) R_{SEI} and (f) R_{CT}.

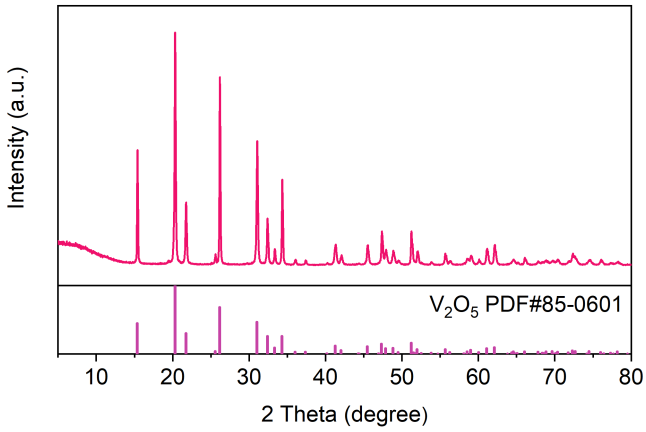

Supplementary Fig. S47 XRD pattern of V_2O_5 cathode material.

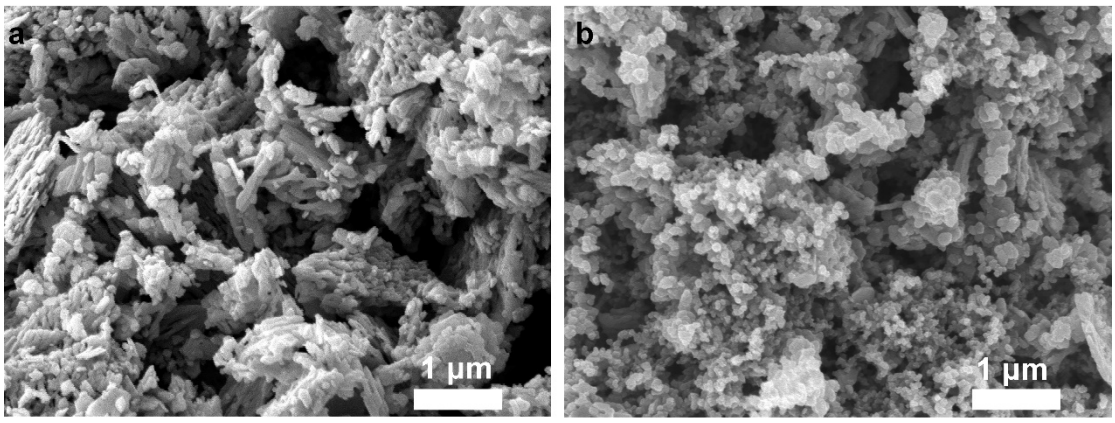

Supplementary Fig. S48 SEM images of V_2O_5 powder (a) before and (b) after coated on carbon paper.

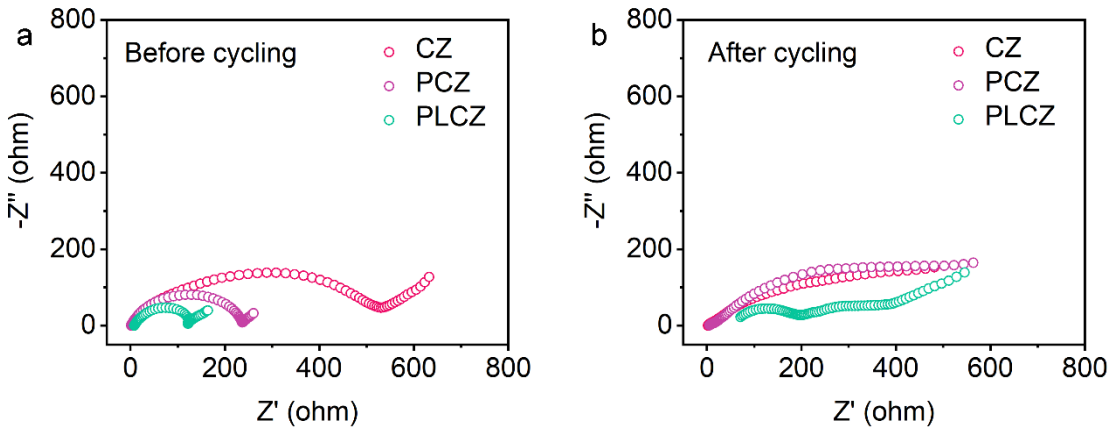

Supplementary Fig. S49 EIS plots of Zn||V_2O_5 with CZ, PCZ and PLCZ electrolytes (a) before and (b) after cycling.

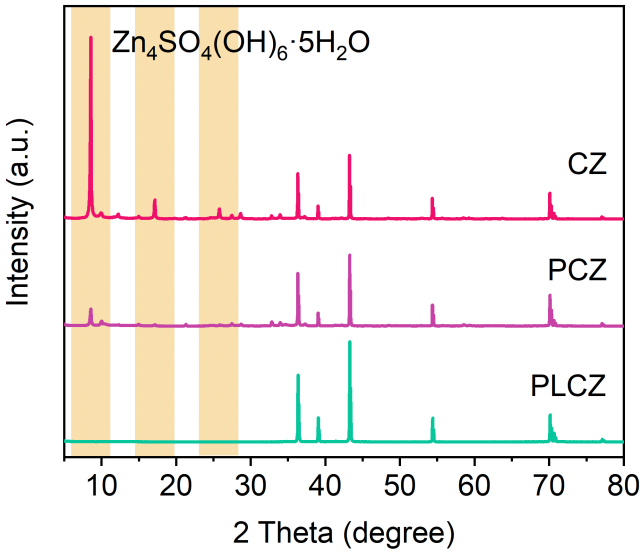

Supplementary Fig. S50 XRD patterns of Zn anodes in Zn||V_2O_5 full cells with CZ, PCZ and PLCZ. After cycling, the CZ and PCZ electrolytes generate a mass of $Zn_4SO_4(OH)_6·5H_2O$ by-product on Zn anodes compared with the PLCZ.

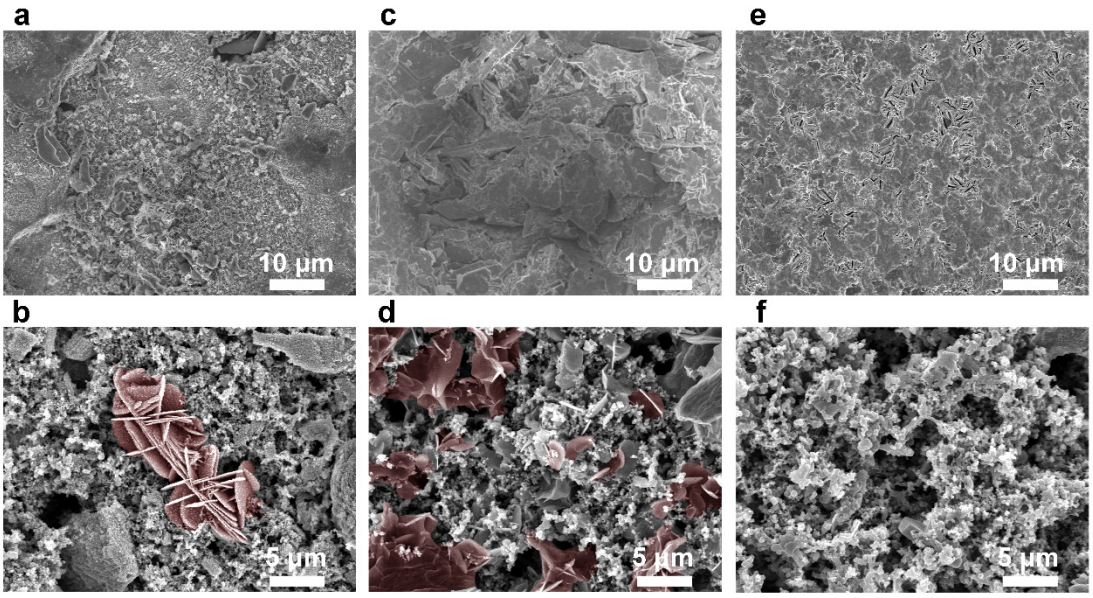

Supplementary Fig. S51 SEM images of Zn anode and V_2O_5 cathode after cycling with (a, b) CZ, (c, d) PCZ, and (e, f) PLCZ. The colored regions represent the formed Zn dendrites on the V_2O_5 cathode surface.

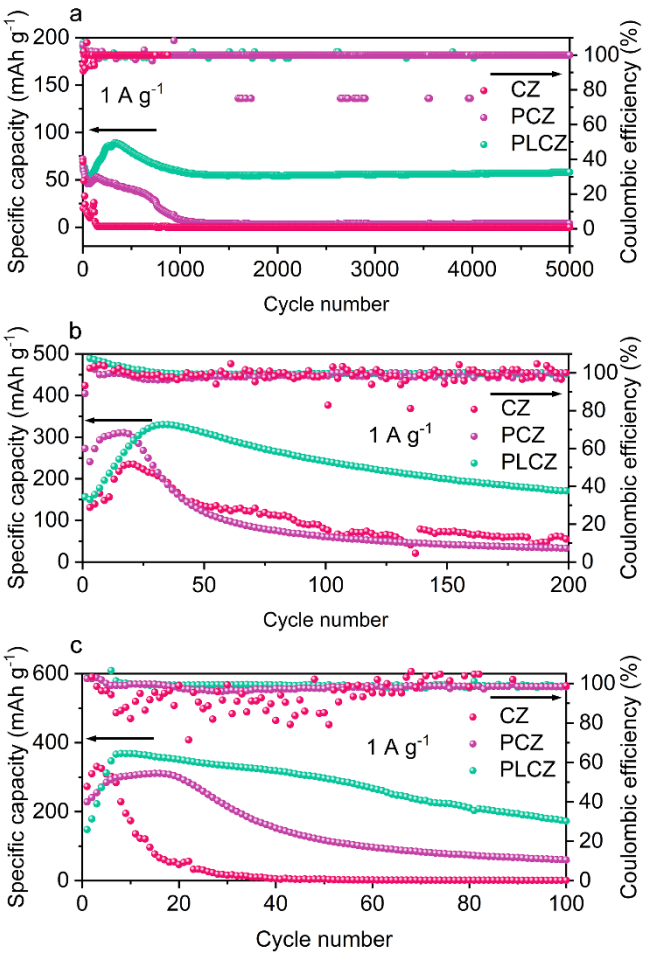

Supplementary Fig. S52 The discharge-charge cycling performances of Zn||V_2O_5 cells with different electrolytes at various temperatures of (a) 273.15, (b) 313.15 and (c) 333.15 K.

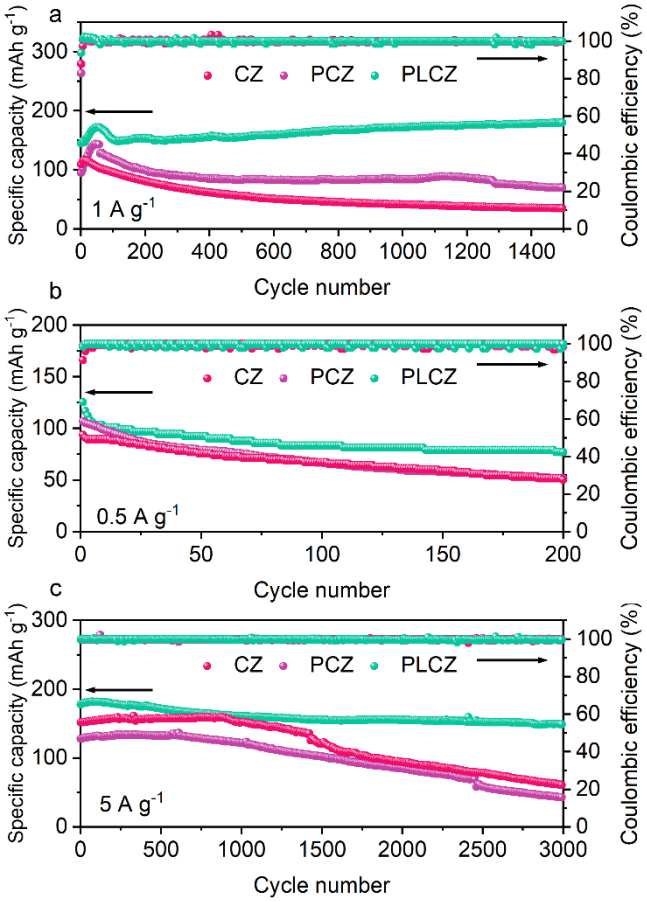

Supplementary Fig. S53 The discharge-charge cycling performances of (a) Zn||MnO_2, (b) Zn||$LiFePO_4$ and (c) Zn||$(NH_4)_2V_{10}O_{25}\cdot 8H_2O$ full cells with different electrolytes. MnO_2 and $LiFePO_4$ were purchased from commercial sources and used without further purification. For the preparation of $(NH_4)_2V_{10}O_{25}\cdot 8H_2O$, 8 mmol NH_4VO_3 was dissolved in 100 ml DI water at 343.15 K and 6 mmol thiourea was pour into the solution with stirring to completely dissolve. Then, dilute sulfuric was added to the above solution to the pH of 2. After that, this solution was stirred another 2.5 h at 363.15 K. After cooling down, the dark green precipitate was filtered, washed with deionized water and finally dried in oven. The preparations of MnO_2, $LiFePO_4$ and $(NH_4)_2V_{10}O_{25}\cdot 8H_2O$ cathode electrodes were same with that of V_2O_5 cathode electrode,

except that the active materials were changed to MnO_2, $LiFePO_4$ and $(NH_4)_2V_{10}O_{25}\cdot 8H_2O$.

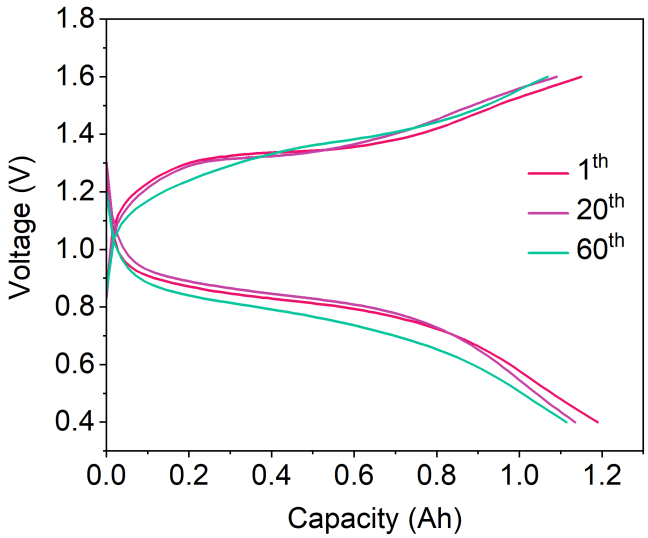

Supplementary Fig. S54 Comparison of cycling performance of pouch cell at different cycles.